Discover Nano

Case Study

Hybrid layer-by-layer assembly of AuNPs/NSF composite for electrochemical detection of miRNA-196a

Jun Ji[1,2] · Gaofan Shi[1,2] · Jiayi Jiang[1,2] · Shu Wu[1,2] · Haoyuan Su[1,2] · Hongzhi Pan[1] · Dongdong Zeng[1]

Received: 29 July 2024 / Accepted: 14 October 2024
Published online: 26 November 2024

Abstract
Detection of microRNA-196a (miRNA-196a) is crucial in cancer research, enabling early diagnosis and providing guidance for individualized treatment. In this work, we employed a naturally occurring negatively charged nano silk fibroin (NSF) with high mechanical properties, biocompatibility, and conductivity to be encapsulated with a positively charged gold nanoparticles (AuNPs) were used as film-forming materials for electrostatic layer-by-layer self-assembly to modify the working electrode of the screen-printed carbon electrode (SPCE). Under the optimized experimental conditions, the uniformly distributed AuNPs on the surface of the multilayer film modified SPCE $(AuNPs/NSF)_{5.5}$/SPCE combined with the sulfhydryl-modified capture probe cp-DNA through gold-sulfur bonds. Furthermore, miRNA-196a is specifically captured through complementary base pairing to achieve highly sensitive and specific detection. $(AuNPs/NSF)_{5.5}$/SPCE electrode can detect miRNA-196a in a concentration range of 1.0×10^{-13} to 1.0×10^{-6} M, and the calculated detection limit is 4.63×10^{-14} M when the signal-to-noise ratio is 3. The obtained results showed that the $(AuNPs/NSF)_{5.5}$/SPCE has excellent selectivity and good stability over time.

Keywords Electrochemical biosensor · Layer-by-layer self-assembly · Gold nanoparticles · Nano silk fibroin · MiRNA-196a

1 Introduction

MicroRNAs (miRNAs), typically ranging from 19 to 24 nucleotides in length, are endogenous non-coding RNAs that play a pivotal role in post-transcriptional gene expression regulation and serve as crucial biomarkers for diagnosing and treating various diseases [1, 2]. Therefore, the establishment of accurate and rapid miRNA detection methods is crucial for the early diagnosis and subsequent treatment of related diseases.

Currently, several sensitive miRNA detection methods have been developed, involving microarray techniques, real-time reverse transcription polymerase chain reaction (RT-PCR), high-throughput sequencing techniques, fluorescence-based biosensors, northern blotting, and electrochemistry [3–9]. While RT-PCR offer high sensitivity and quantitative measurement capabilities, they are hindered by their requirements for expensive instrumentation and specialized expertise [10]. Similarly,

Jun Ji and Gaofan Shi are co-first authors.

Supplementary Information The online version contains supplementary material available at https://doi.org/10.1186/s11671-024-04127-0.

✉ Hongzhi Pan, panhongzhi@163.com; ✉ Dongdong Zeng, zengdd@sumhs.edu.cn | [1]Shanghai University of Medicine and Health Sciences, Shanghai 201318, China. [2]University of Shanghai for Science and Technology, Shanghai 200093, China.

northern blotting, despite its capacity for multiplexed detection and size determination of miRNAs, is labor-intensive and comparatively less sensitive. MiRNA array technologies, though facilitating simultaneous profiling of multiple miRNAs, are complex and costly. In contrast, electrochemical detection of miRNAs combined several advantages, including high sensitivity, rapid analysis, cost-effectiveness, portability, and label-free detection [11]. These attributes position electrochemical methods as promising alternatives for miRNA analysis, with potential implications for both research and clinical diagnostics.

To enhance sensitivity, selectivity, and reduce detection limits, modifications of bare electrodes are commonly employed. The introduction of nanomaterials has played a crucial role in further improving the analytical performance of electrochemical sensors, specifically in terms of electron transfer rates and electrocatalytic abilities [12–14]. Zhuang et al. developed a gold electrode (AuE) modified with gold nanoparticles (AuNPs) and coupled with a DNA capture probe for the detection of miRNA-100 in the serum of gastric cancer patients [15]. The study demonstrated uniform deposition of AuNPs on the AuE surface, resulting in enhanced conductivity and effective surface area. However, for applications requiring a larger specific surface area, AuNPs may have limitations [16, 17]. To address these limitations, researchers often employ composites or incorporate additional functional nanomaterials to augment both the specific surface area. Silk fibroin has found widespread application in electrochemical biosensors, demonstrating high-performance detection capabilities for glucose, nitroaniline, pH, and pressure sensing [18–21]. Notably, the exploration of mildly extracted nano silk fibroin (NSF) in synergy with other materials for the fabrication of electrochemical biosensors remains unreported. However, the catalytic activity of NSF may be restricted, potentially leading to sensors that are less sensitive than anticipated [22]. NSF may demonstrate reduced catalytic efficiency and reaction rates during electrocatalysis.

The conventional fixation approach for electrochemical biosensors typically involves a mixed coating of various materials. This method presents limitations: firstly, it only allows for the control of thin film growth on a two-dimensional plane; secondly, it struggles to harness the unique advantages of materials and may even compromise their inherent properties [23–25]. Yin et al. prepared a AuNPs/silk fibroin (SF) modified glassy carbon electrode for the immobilization of horseradish peroxidase (HRP) [26]. Although this method was able to immobilize HRP and maintain its biological activity to a certain extent, the nanoparticles aggregated under some conditions and these aggregations could lead to a significant loss of electrocatalytic capacity [27, 28]. In contrast, layer-by-layer self-assembly represents a nanotechnology for constructing intricate structures through the sequential stacking of materials. This process encompasses surface modification, the application of layer-by-layer self-assembled material solutions to a substrate, layer-by-layer interactions, multiple iterations of adding layers, and a termination step to ensure the completion of self-assembly. Layer-by-layer self-assembly stands out for its high flexibility and precision, effectively amalgamating the exceptional properties of multiple materials to compensate for individual material deficiencies while enhancing specific functions [29, 30]. Although spray coating and spin spray methods can expedite the deposition of thin film layers within seconds, their reliance on expensive instruments and intricate setup adjustments hampers the widespread application of layer-by-layer self-assembly. Therefore, attaining an equivalent-quality thin layer system in a shorter timeframe becomes imperative for practical applications.

In this work, AuNPs and NSF were modified on screen-printed carbon electrode (SPCE) by layer-by-layer self-assembly to serve as a sensing interface for the specific detection of miRNA-196a. Scheme 1 showed the modification process of the electrochemical sensor. AuNPs and NSF were modified layer-by-layer on the electrode surface by electrostatic interaction between the two materials. The platform combines the high electrocatalytic ability of AuNPs and the high active area of NSF to improve the adsorption performance of biomolecules. The biorecognition mechanism of this experiment was based on the specific interaction between capture DNA and miRNA-196a. When the capture probe was present, miRNA-196a was captured onto the modified electrode, hindering electron transfer and reducing the peak response of the DPV current. The biosensor developed in this study can be used as a low-cost, specific and sensitive strategy for early clinical cancer detection compared to conventional detection methods.

2 Experimental section

2.1 Reagents and chemicals

Human serum samples are provided by Shanghai Pudong new area Zhoupu hospital. All reagents except silkworm cocoons were used directly in this study. Silkworm cocoons were purchased from Northwest Sericulture Base. Sodium hydroxide, urea, anhydrous sodium bicarbonate, potassium ferrocyanide ($K_4[Fe(CN)_6]$), potassium ferricyanide ($K_3[Fe(CN)_6]$), tris(2-carboxyethyl)phosphine (TCEP), mercaptoethanol (MCH) was purchased from Shanghai Titan Technology Co., Ltd. Chlorauric acid ($HAuCl_4 \cdot 3H_2O$) and tetraoctylammonium bromide (TOABr) were purchased from

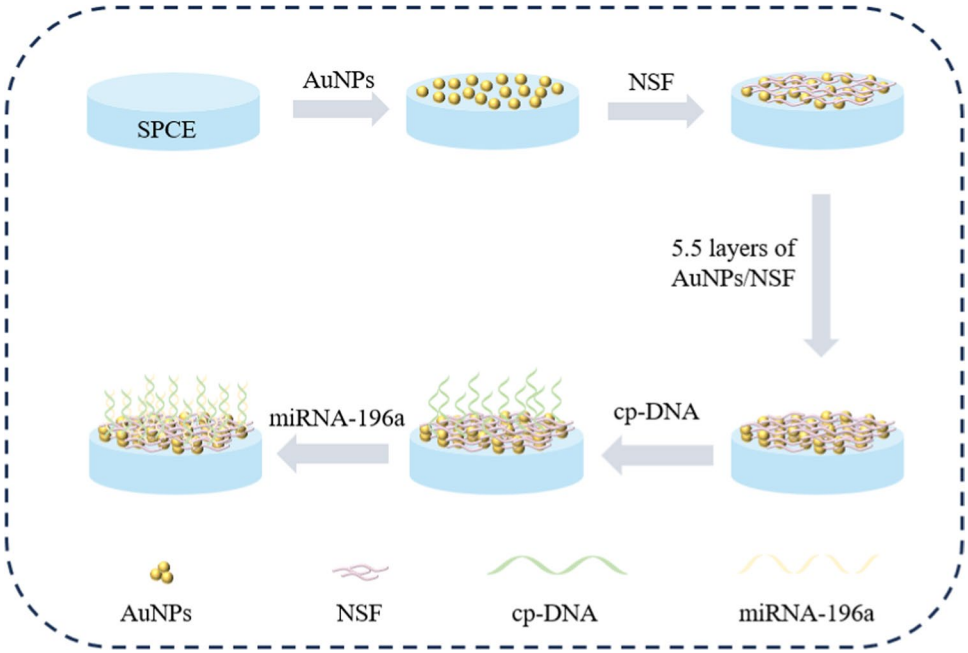

Scheme 1 Schematic of the electrochemical biosensor based on $(AuNPs/NSF)_{5.5}$/SPCE for detection of miRNA-196a

Shanghai Acmec Biochemical Co., Ltd. Sodium borohydride ($NaBH_4$) was purchased from Sinopharm Chemical Reagent Co., Ltd. diethyl pyrocarbonate (DEPC) water and phosphate buffer saline (PBS) were purchased from Sangon Biotech Co., Ltd. DNA and miRNA were synthesized by Sangon Biotechnology, and the sequences are shown in Table 1.

2.2 Experimental apparatus

Electrochemical experiments were carried out on CHI660B (Shanghai Chenhua Instrument, China) with a three-electrode system, which contained carbon, Ag/AgCl and platinum (Pt) as working, reference and counter electrode respectively. Scanning electron microscope (SEM, Regulus 8100, Guoyi Quantum Technology Co., Ltd., China) was used for microstructure characterization. All electrochemical measurements were conducted in 0.1 M KCl solution containing 5 mM $[Fe(CN)_6]^{3-/4-}$ used as an electrolyte in the potential range of – 0.2 to 0.6 V.

2.3 Synthesis of 4-(dimethylamino)pyridine-gold nanoparticles composites

4-(Dimethylamino)pyridine (DMAP) capped gold nanoparticles (AuNPs) composites were prepared by phase transfer method. Briefly, after adding $HAuCl_4$ aqueous solution to TOABr toluene solution, the $HAuCl_4$ nanoparticles were transferred from the aqueous phase to the toluene phase after magnetic stirring for 30 min, and $NaBH_4$ aqueous solution was added to the mixed solution to reduce the $HAuCl_4$ nanoparticles to AuNPs. The upper toluene solution was taken, and then DMAP solution was added to the toluene phase and stirred for 24 h. At this point, the AuNPs were capped by DMAP and transferred to the toluene phase, where the AuNPs were capped by DMAP and transferred to the toluene phase. The AuNPs were then capped by DMAP and transferred to the aqueous phase. The aqueous solution was collected, and the solution used in the experiment was obtained by diluting this solution 10 times. The

Table 1 DNA and miRNA sequences

Name	Sequence (5′ to 3′)
cp-DNA	SH-CCCAACAACATGAAACTACCTA
miRNA-196a	UAGGUAGUUUCAUGUUGUUGGG
miRNA-21	UAGCUUAUCAGACUGAUGUUGA
miRNA-155	UUAAUGCUAAUCGUGAUAGGGGU
miRNA-210	AGCCCCUGCCCACCGCACACUG

UV–Vis absorption spectra confirmed the successful preparation of AuNPs, and the absorption band around 520 nm indicated the reduction of AuNPs.

2.4 Extraction of NSF

The extraction of NSF involves several steps: silk degumming, dissolution, dialysis, ultrasonication, centrifugation, and freeze-drying [31] (Fig. S1).

Initially, 2 L of Na_2CO_3 aqueous solution, characterized by a mass fraction of 0.5 wt%, is heated to its boiling point. Subsequently, 15 g of silkworm cocoons, free from silkworm chrysalis and impurities, are excised and immersed in the aforementioned solution. The mixture is then subjected to 30 min of heating, with concurrent stirring facilitated by a glass rod to facilitate silk degumming. The silk was then thoroughly washed three times and wrung dry. The primary degummed silk is introduced into the boiling Na_2CO_3 aqueous solution for a subsequent 30 min heating cycle, employing identical conditions for the second degumming phase. The silk is then washed thrice with ultrapure water and left to dry at room temperature for 24 h, resulting in the acquisition of degummed silk. Weigh 3 g of degummed silk and add it to 100 g of pre-cooled NaOH/urea aqueous solution in a – 20 °C refrigerator. Stir the solution at room temperature for 10 min every 12 h, repeating this process for 3 days to achieve complete silk dissolution. Transfer the dissolved silk solution into a dialysis bag and place it in a beaker filled with 1 L of ultrapure water for 3 days, changing the water every 12 h to remove salt ions. Subsequently, subject the dialyzed silk fiber mixture to a 30-min ultrasonic treatment in ice water (400 W) to extract NSF. Centrifuge the mixture at 6000 r/min for 20 min, retaining the supernatant. Freeze 20 mL of the supernatant at – 80 °C for 8 h, followed by freeze-drying for 48 h to obtain the freeze-dried NSF.

2.5 Preparation of $(AuNPs/NSF)_n$ modified SPCE

The $(AuNPs/NSF)_n$ film is assembled through electrostatic layer-by-layer self-assembly on SPCE. Prior to use, the SPCE undergo treatment with a plasma cleaning agent to render their surfaces hydrophilic, incorporating negatively charged hydroxyl groups. The subsequent electrostatic interaction between the electrode surfaces and the electrolyte propels the self-assembly process. Initiating the procedure involves the meticulous addition of 3 µL of a tenfold diluted AuNPs solution (pH 11.0) dropwise onto the working electrode, followed by a rinse with deionized water after 10 min. Subsequently, the NSF solution (pH 9.0) is added dropwise, and after 10 min, it is rinsed with deionized water of the same pH to ensure proper rinsing. The electrodes are then dried with N_2. Repetition of this sequence results in sixteen-channel SPCE modified with multi-thin films. Concurrently, to establish a binding site between cp-DNA and AuNPs, an additional layer of AuNPs is constructed atop the $(AuNPs/NSF)_n$ multilayer film, denoted as $(AuNPs/NSF)_{n.5}$.

2.6 Fabrication of biosensing platform

Coupling of cp-DNA to AuNPs in this experiment was achieved through gold-sulfur bonding. Cp-DNA (1 µM) is applied to the prepared working electrode, stored in a humid box at 4 °C for 12 h, and then gently washed with DEPC water, followed by drying with N_2. Subsequently, 3 µL of a 2 mM MCH solution (containing 2 mM TCEP) is added to the electrode, stored in a humid box at room temperature for 1 h to block unbound sites and prevent non-specific adsorption. Unbound MCH is gently washed off with 10 mM PBS, followed by drying with nitrogen. MiRNA solutions of various concentrations are added dropwise, and the system is incubated in a refrigerator at 4 °C for 5 h to facilitate hybridization. Finally, unhybridized miRNA strands are gently washed off with DEPC water, and the electrode is dried using N_2.

3 Results and discussion

3.1 Characterization and electrochemical behavior of electrodes

The surface morphology of the modified electrodes was characterized by scanning electron microscopy (SEM). As shown in Fig. 1A–C, the surface morphology of the bare electrode, NSF and AuNPs mixed coating modified SPCE, and (AuNPs/

$NSF)_5$ modified SPCE were examined through SEM. As shown in Fig. 1A, the bare SPCE has a large surface morphology but lack binding sites for biomarkers. For the mixed-coating of AuNPs and NSF (Fig. 1B), the film formation was uneven and the AuNPs appeared to be agglomerated, limiting the full utilization of their material properties. In contrast, $(AuNPs/NSF)_5$/SPCE (Fig. 1C), where AuNPs are uniformly dispersed on NSF. The synergistic effect of NSF and AuNPs enhances the specific surface area and electrocatalytic properties of the electrodes. The specific surface area of the NSF modified electrode is small, and some of the NSF curls into clusters, forming protrusions on the electrode surface (Fig. S2).

The electrochemical behaviors of electrodes modified with different materials have been investigated by cyclic voltammetry (CV), and the results of which were as shown in Fig. 1D. The anode peak current for the bare SPCE and mixed coating electrode were determined as 38.89 µA and 56.06 µA respectively. The results clearly showed that casting AuNPs and NSF onto the bare SPCE surface helped to increase the peak current, as AuNPs and NSF have excellent electrocatalytic properties and specific surface area. As anticipated, the peak current of $(AuNPs/NSF)_5$/SPCE had gone up to 76.65 µA following the layer-by layer self-assembly of AuNPs and NSF on the SPCE surface, indicating that the layer-by-layer self-assembly of AuNPs and NSF increased the surface area of electrode. Compared with the previous two electrodes, the electrode modified with $(AuNPs/NSF)_5$ represent the best current response, indicating that the layer-by-layer self-assembly of AuNPs and NSF accelerated electron transfer. The Randles–Sevcik formula was used to estimate the effective surface area of different modified electrodes. The surface area of the $(AuNPs/NSF)_5$/SPCE was estimated to be 0.0696 cm^2, which is larger than bare SPCE (0.0353 cm^2) and mixed coating electrode (0.0509 cm^2). Obviously, $(AuNPs/NSF)_5$/SPCE has the large effective surface area, which provides more catalytic sites for capture probe, consequently improving the current response.

Electrochemical impedance spectroscopy (EIS), consisting of a semicircular part and a linear part, was used to characterize the interfacial properties of different modified electrodes. As displayed in Fig. 1E, the bare SPCE showed R_{ct} value

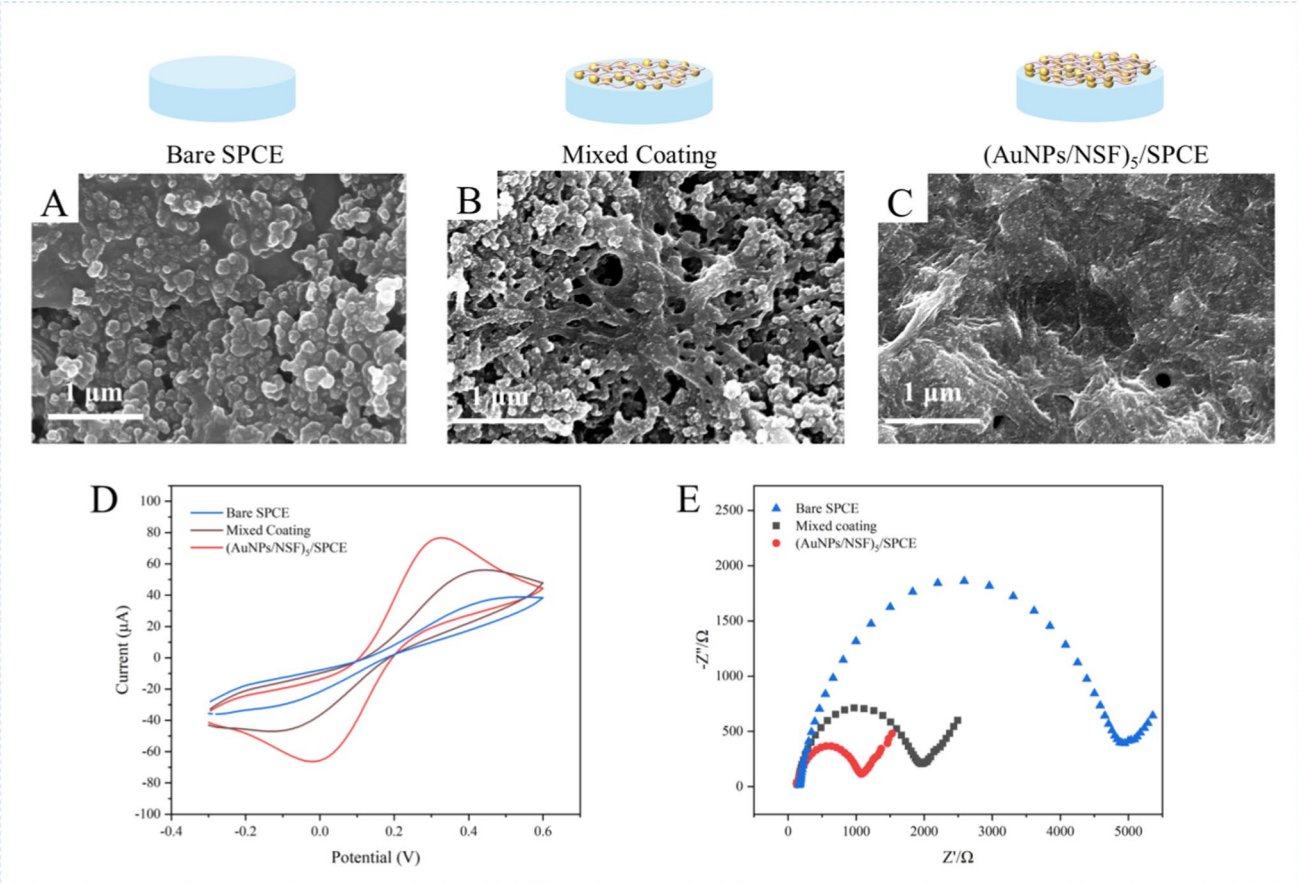

Fig. 1 SEM images of bare SPCE (**A**), mixed coating (**B**) and $(AuNPs/NSF)_5$/SPCE (**C**). **D** CV curves of SPCE, mixed coating and $(AuNPs/NSF)_5$/SPCE. **E** EIS changes of bare SPCE, mixed coating and $(AuNPs/NSF)_5$/SPCE. All the above electrochemical experiments were performed in 100 mM KCl containing 5 mM $[Fe(CN)_6]^{3-/4-}$ at a scanning rate of 100 mV/s

of 4945 Ω, while a significant decrease in R_{ct} was observed on mixed-coating (R_{ct} = 1958 Ω). Owing to large effective surface areas and electrical conductivity, mixed-coating of AuNPs and NSF promotes charge transfer rate between the electrode and $[Fe(CN)_6]^{3-/4-}$ electroactive pairs. It was worth noting that the R_{ct} was further decreased to 1071 Ω after the layer-by-layer self-assembly of AuNPs and NSF on the surface of SPCE, indicating that the nanocomposite material effectively improved electrochemical activity and had higher conductivity (Fig. 1E). To summarize, $(AuNPs/NSF)_5$/SPCE demonstrated excellent electrocatalytic ability and conductivity.

Fourier infrared spectroscopy and zeta potential instrumentation were used to determine the structural characteristics of the proteins in the extracted NSF solutions and the stability of the suspensions (Fig. S3). As shown in Fig. S3A, the transmission spectra showed the characteristic peaks from the peptide bond –CONH– for amide I, amide II, and amide III. The structural characteristic peaks at 1620 cm^{-1} corresponded to the –C=O– and –N–H-bonds in the amide I, and the congruent combination of characteristic peaks for the –C=O– and –C–N-bonds (located at 1517 cm^{-1} and 1229 cm^{-1}, respectively) correspond to the amide II and amide III regions, respectively. As shown in Fig. S3B, the Zeta potential of NSF showed a significant negative charge, and the Zeta potential of NSF suspension was – 30.4 mV. Since the absolute value of the Zeta potential was greater than 30 mV, it indicated that the exfoliated NSF was more negatively charged, the intermolecular electrostatic repulsion was larger, and the stability of NSF suspension was better. In addition, in response to the FTIR spectra and the available amino acid sequences in filipin proteins, we hypothesized that the amino acids in NSF are mainly composed of glycine (Gly), alanine (Ala), serine (Ser), and its basic structure is shown in Fig. S3C. The elemental composition of $(AuNPs/NSF)_5$/SPCE was shown in Fig. S4. The kinetic of the $(AuNPs/NSF)_5$/SPCE reaction was under further investigation by CV at a scan rate (v) of 10–150 mV/s. As shown in Fig. S5A, B, the intensity of anodic peak currents of the modified electrode varied linearly with increasing square root of the scan rate. The corresponding fitting equation was $y = 6.03x + 10.22$ ($R^2 = 0.9964$). This result demonstrated that the electrochemical catalytic reaction on the electrode surface was a diffusion-controlled process [32].

3.2 Optimization of experimental conditions

The optimization of experimental conditions holds critical importance in amplifying the electrochemical signals of the electrode. In this study, we methodically optimized several pivotal factors influencing the chemical reaction rate on the electrode surface. These factors include the pH of the NSF solution, the quantity of assembled layers of the AuNPs/NSF on the electrode, and the duration of the quartz slide immersed in the solution [33–36].

The pH would affect the degree of ionization and the net charge of the electrolyte, thereby affecting the adsorption between layers of electrostatic layer-by-layer self-assembled films. This experiment investigated the effects of three pH of NSF solution on the adsorption of multilayer films, respectively pH 7.0, 9.0 and 11.0. In the experiment, the absorbance of n = 1, 3, 5, 7, and 9 layers of film was measured. Figure 2A selects the absorbance curve of n = 1, 5, and 9 layers of film to plot. It can be seen from the figure that the NSF of the UV absorbance increases with the number of layers. As shown in Fig. 2B, absorbance has a linear correlation with the number of layers. The slopes of the linear equations are 0.00765, 0.0084, and 0.0039, representing the amount of film adsorption (x is the number of layers). Absorbance increases with the number of layers and was larger for the NSF solution at pH 9.0 than for the other two. Therefore, it can be judged that pH 9.0 is a more suitable for the NSF solution at which adsorption is faster.

We optimized the immersion time for the preparation of $(AuNPs/NSF)_3$ and $(AuNPs/NSF)_5$ on quartz slides, monitoring absorbance changes of the films at various immersion times using a UV–visible spectrophotometer (UV–Vis) to indicate film thickness. The absorbance-time curves presented in Fig. S6 demonstrate a rapid increase in absorbance within the initial 300 s, followed by a stable phase with no significant changes thereafter. This pattern suggests that the adsorption capacity of the film reaches saturation around the 300-s mark. Guided by the time-absorbance curves for both multilayers, we determined 300 s as the optimal soaking time for subsequent experiments. It is noteworthy that the number of AuNPs/NSF layers directly influences the analytical sensing performance of the electrode. As illustrated in Fig. 2C, the current response signal intensity of AuNPs/NSF with different layers displays variations, characterized by an initial ascent followed by a subsequent decrease. The reduction in current response signal may arise from impeded electron transfer with relatively thick films, hindering optimal signal transmission. The oxidation peak current signal intensity exhibits a significant increase from 1 to 5, undergoes a slight decrease at 6, and experiences a rapid decline from 7 onwards (Fig. 2D). Consequently, n = 5 was identified as the optimal number of $(AuNPs/NSF)_n$ for subsequent experiments.

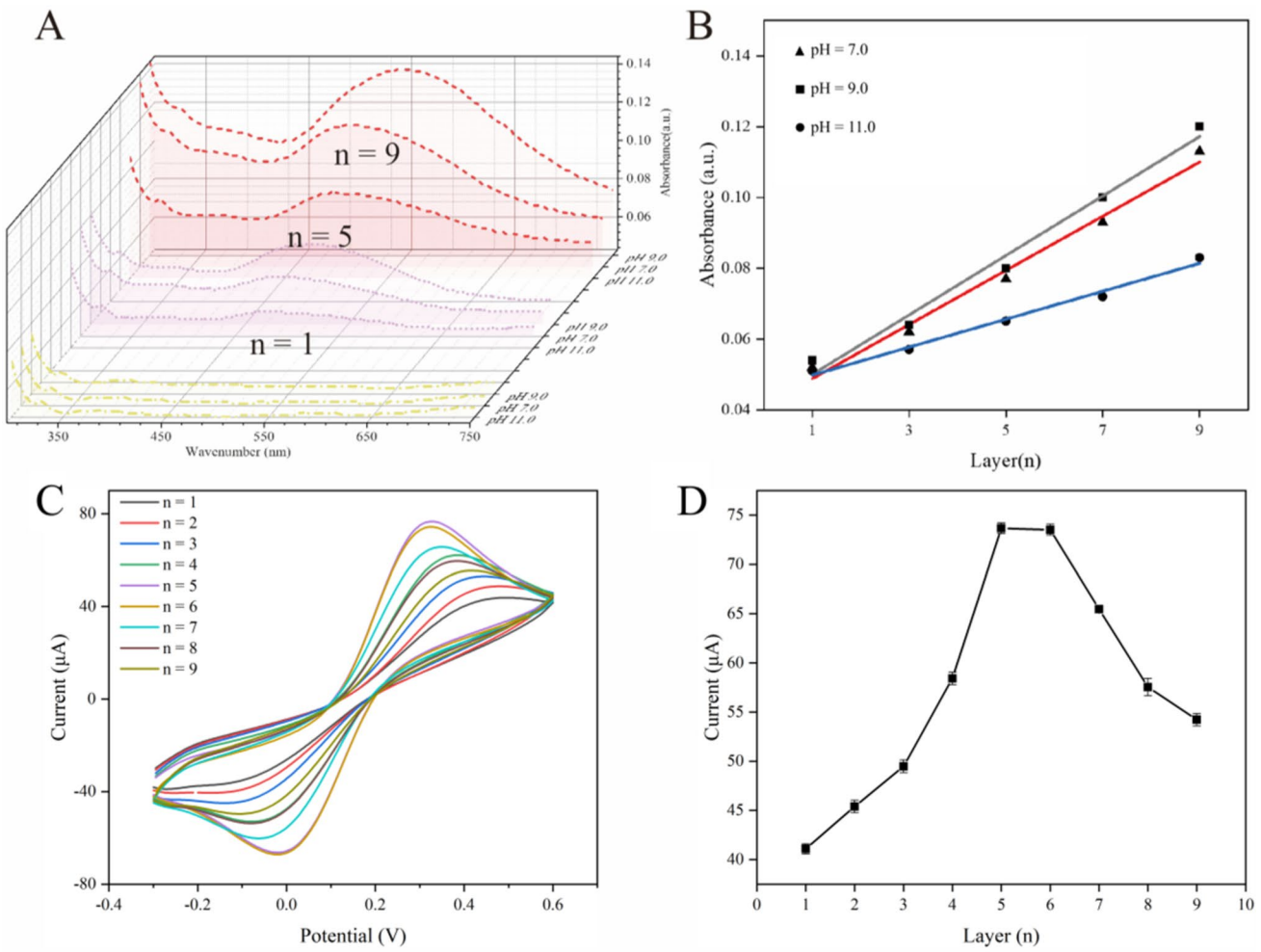

Fig. 2 **A** Effects of NSF solution pH for assembly of $(AuNPs/NSF)_n$; **B** Linear relationship between absorbance and $(AuNPs/NSF)_n$ of NSF with different pH. Linear regression equation: $y = 0.00765x + 0.0412$, $R^2 = 0.982$ (pH = 7.0), linear regression equation: $y = 0.0084x + 0.0416$, $R^2 = 0.980$ (pH = 9.0), linear regression equation: $y = 0.00395x + 0.459$, $R^2 = 0.985$ (pH = 11.0); **C** CV curves of electrodes modified with different layers of $(AuNPs/NSF)_n$; **D** Variation curve of oxidation peak current with $(AuNPs/NSF)_n$. All the above electrochemical experiments were performed in 100 mM KCl containing 5 mM $[Fe(CN)_6]^{3-/4-}$ at a scan rate of 100 mV/s

3.3 Detection performance of miRNA-196a

$(AuNPs/NSF)_{5.5}$/SPCE was prepared on the basis of $(AuNPs/NSF)_5$ in order to allow cp-DNA and AuNPs to bind through gold-sulfur bonds. In this study, we investigated DPV responses of the $(AuNPs/NSF)_{5.5}$ modified electrochemical biosensor to different target concentrations of miRNA-196a, and the selectivity, stability, and reusability of electrochemical biosensors to interfering substances. DPV parameters are set respectively: step potential is 0.004 V, the modulation amplitude is 0.05 V, and the pulse width is 0.05 s.

When the cp-DNA of miRNA-196a binds to the uniform AuNPs on the multilayer film's surface via gold-sulfur bonds and forms a duplex with miRNA-196a through complementary base pairing, it induces an increase in the surface resistance of the electrode, resulting in a decrease in the oxidation peak current signal. The amount of adsorption is directly related to the change in signal value. As depicted in Fig. 3A, a distinct oxidation peak of $[Fe(CN)_6]^{3-/4-}$ is observed at 0.2 V. As the negative logarithm of the concentration of miRNA-196a increases, the oxidation peak current correspondingly rises. The linear curve is represented as $y = 2.079x - 4.453$ ($R^2 = 0.998$), where x denotes the negative logarithm of the concentration of miRNA-196a in mol/L, and y represents the current signal value in μA (Fig. 3B). The calculated detection limit (LOD) for the constructed sensor is 4.63×10^{-14} M (S/N = 3).

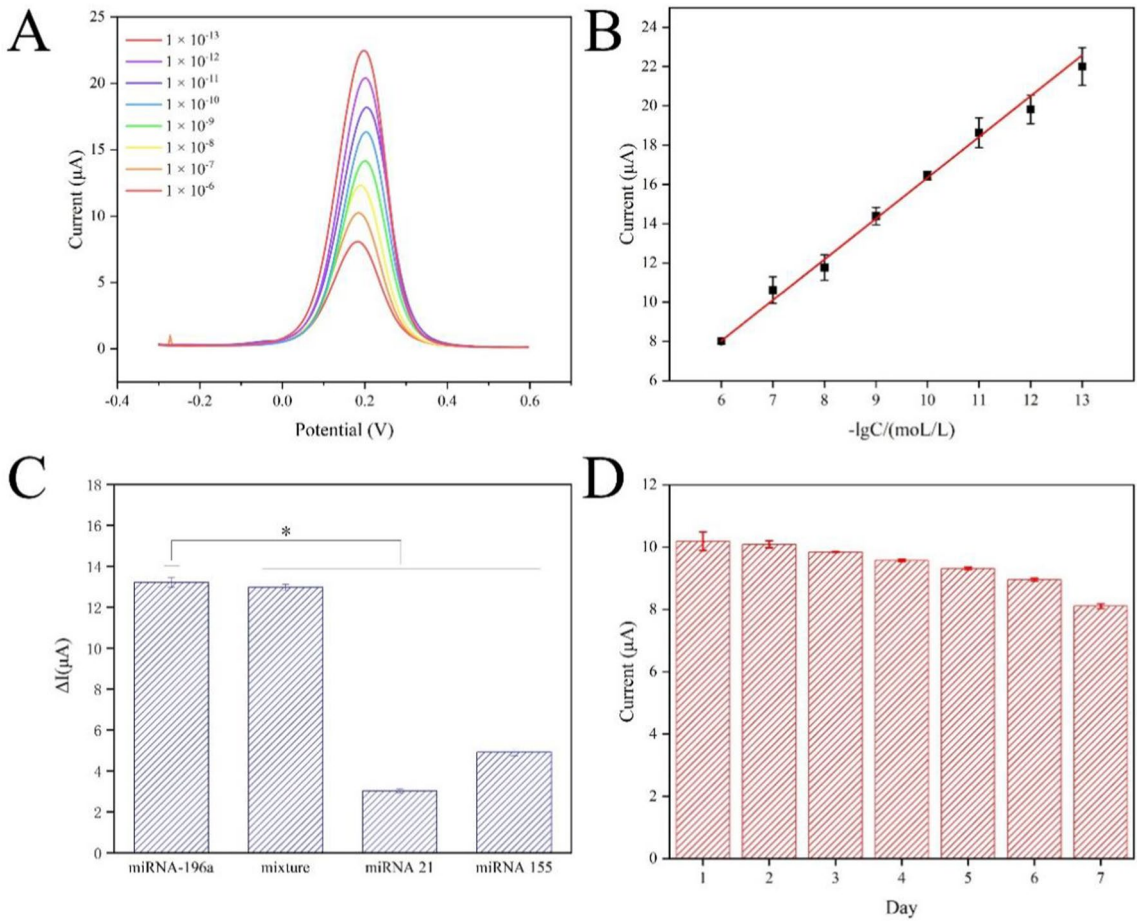

Fig. 3 **A** DPVs of $(AuNPs/NSF)_{5.5}$/SPCE with different concentrations of miRNA-196a: 1×10^{-13} to 1×10^{-6}. **B** The oxidation peak current is linearly correlated with logarithm of the concentration of miRNA-196a. Linear regression equation: $y=2.079x-4.453$ ($R^2=0.998$). **C** Selectivity of electrochemical biosensors to interfering substances. Error bars represented standard deviation (n = 3). Statistical analysis: $^*p<0.05$. **D** Stability of electrochemical biosensor for detection of miRNA-196a within 7 days. Error bars represented standard deviation (n = 3)

Selectivity and stability are pivotal properties that determine the practical application potential of electrochemical biosensors. In this study, initial assessments were conducted to evaluate the changes in DPV current response of $(AuNPs/NSF)_{5.5}$/SPCE upon exposure to miRNA-196a, miRNA-196a and miRNA-21 mixture, miRNA-21, and miRNA-155, each at a concentration of 1×10^{-9} M (Fig. 3C). Notably, a significant change in current signal is observed solely in the presence of miRNA-196a, demonstrating high selectivity. Simultaneously, the $(AuNPs/NSF)_{5.5}$/SPCE was stored at 4 ℃, and environmental stability was assessed over a 7-day period (Fig. 3D). The oxidation peak current signal of the $(AuNPs/NSF)_{5.5}$ modified electrode exhibited a decrease within 7 days, with a relative standard deviation (RSD) of 7.43%, indicating robust stability of the electrochemical biosensor. As shown in Fig. S7, the anti-interference performance of the biosensor was performed at a concentration of 1×10^{-7} M. As shown in Table 2, compared to other label-free electrochemical biosensors for miRNA detection, the proposed electrochemical biosensor showed wider linear range and lower detection limit.

The practicability of the prepared electrochemical biosensor was evaluated by standard addition method. Specifically, normal human serum samples were taken and diluted 100-fold by adding 0.01 M PBS solution. The above serum dilution was added to miRNA-196a as a base solution, and miRNA-196a serum solutions with concentrations of 1.0×10^{-7}, 1.0×10^{-9} and 1.0×10^{-11} M were respectively prepared. The recoveries of the three concentrations of miRNA-196a solutions are shown in Table 3, the recoveries are between 89.1 and 114% and the relative standard deviation RSD is within 15%. Finally, we evaluated the reusability of $(AuNPs/NSF)_5$/SPCE. As shown in Fig. S8, the current signal was observed higher after denaturing the cp-DNA, and back to the level of the origin intensity after incubating with miRNA-196a again. These results indicated the potential reusability of the $(AuNPs/NSF)_5$/SPCE.

Table 2 The performance comparison of electrochemical biosensors for detecting miRNA

Type	Material	Capture probe	Detection limit	Linear range	References
Labeled biosensor	AuNPs	Ferrocene/methylene blue/cp-DNA	33 fM	100 fM–100 nM	[37]
	AuNPs/Graphitic carbon nitride nanosheets	Ferrocene/DNAzyme walker	4.3/78.6 aM	100 aM–100 nM	[38]
	Magnetic Nanoparticles/	Biotin/cp-DNA	0.27 aM	1 aM–1 pM	[39]
Label-free biosensor	MXene	Tetrahedral DNA nanostructures	5 pM	5 pM–10 nM	[40]
	poly($_L$-cysteine)/MoS_2	probe DNA	78 fM	100 fM–1 nM	[41]
	ZIF-8/AuNPs	3D DNA walker	29 pM	0.1 nM–10 μM	[42]
	AuNPs/NSF	cp-DNA	46.3 fM	0.1 pM–1 μM	This work

Table 3 Detection of miRNA-196a in serum samples

Sample number	Group number	Sample concentration (M)	Measured concentration (M)	Recovery rate (%)	RSD (%)
Serum 1	1	1.0×10^{-7}	8.95×10^{-8}	89.5	4.98
	2	1.0×10^{-7}	8.47×10^{-8}	84.7	
	3	1.0×10^{-7}	9.36×10^{-8}	93.6	
Serum 2	1	1.0×10^{-9}	1.01×10^{-9}	101	9.14
	2	1.0×10^{-9}	1.09×10^{-9}	109	
	3	1.0×10^{-9}	8.91×10^{-10}	89.1	
Serum 3	1	1.0×10^{-11}	1.14×10^{-11}	114	13.02
	2	1.0×10^{-11}	9.01×10^{-12}	90.1	
	3	1.0×10^{-11}	1.14×10^{-11}	114	

4 Conclusion

The development of electrochemical biosensors for miRNA-196a detection presents several critical challenges that must be systematically addressed to ensure efficacy. Key among these is ensuring selectivity, given the substantial homology among miRNA sequences. Additionally, sensor stability and reproducibility are major concerns, as AuNP aggregation, NSF degradation, and fabrication inconsistencies can compromise performance. Layer-by-layer self-assembly offers a strategic advantage, allowing precise control over material deposition, enhancing stability, and fine-tuning surface properties. Addressing these challenges, while leveraging this technology, is crucial for advancing reliable sensors for clinical miRNA-196a diagnostics. In conclusion, we developed an electrochemical sensor based on $(AuNPs/NSF)_{5.5}$ for the detection of miRNA-196a. SEM confirmed that AuNPs and NSF were successfully modified on the electrode surface by layer-by-layer self-assembly. It was worth mentioning that the successful modification of the electrode effectively enhanced the stability and electrochemical properties of the sensor. Under the optimal conditions, the sensor had a wide linear range of 1.0×10^{-6} to 1.0×10^{-13} M, a low limit of detection of 4.63×10^{-14} M and spiked recoveries of 89.1–114%. In addition, the sensor exhibited good anti-interference, specificity and stability. This experiment is potentially valuable for the clinical judgment of miRNA-196a-related cancer diseases.

Acknowledgements This work was supported by the Shanghai Municipal Health Commission Research Project plan (202340295).

Author contributions JJ and GS wrote the main manuscript text conducted the investigation and data curation. DZ provided conceptualization and methodology, supervised the project and reviewed and edited the manuscript. JJ also performed the formal analysis. JJ, SW, HS, and HP provided supervision. All authors reviewed the manuscript.

Data availability Data will be made available on request.

Declarations

Ethics approval and consent to participate Participants were informed about the purpose, background, process, risks and benefits of the study and consented to participate in the study. Informed consent was obtained from the parents/ legally authorized representatives of subjects who are under 16.

Competing interests The authors declare that they have no competing interests.

References

1. Saliminejad K, KhorramKhorshid HR, SoleymaniFard S, Ghaffari SH. An overview of microRNAs: biology, functions, therapeutics, and analysis methods. J Cell Physiol. 2019;234:5451–65. https://doi.org/10.1002/jcp.27486.
2. Zhang C, Miao P, Sun M, Yan M, Liu H. Progress in miRNA detection using graphene material-based biosensors. Small. 2019;15:1901867. https://doi.org/10.1002/smll.201901867.
3. Konishi H, Ichikawa D, Arita T, Otsuji E. Microarray technology and its applications for detecting plasma microrna biomarkers in digestive tract cancers. In: Li PCH, Sedighi A, Wang L, editors. Microarray technology. New York: Springer; 2016. p. 99–109. https://doi.org/10.1007/978-1-4939-3136-1_8.
4. McMillan KS, McCluskey AG, Sorensen A, Boyd M, Zagnoni M. Emulsion technologies for multicellular tumour spheroid radiation assays. Analyst. 2016;141:100–10. https://doi.org/10.1039/C5AN01382H.
5. Ban E, Song EJ. Considerations and suggestions for the reliable analysis of miRNA in plasma using qRT-PCR. Genes. 2022;13:328. https://doi.org/10.3390/genes13020328.
6. Jet T, Gines G, Rondelez Y, Taly V. Advances in multiplexed techniques for the detection and quantification of microRNAs. Chem Soc Rev. 2021;50:4141–61. https://doi.org/10.1039/D0CS00609B.
7. Nguyen LD, Wei Z, Silva MC, Barberán-Soler S, Zhang J, Rabinovsky R, Muratore CR, Stricker JMS, Hortman C, Young-Pearse TL, Haggarty SJ, Krichevsky AM. Small molecule regulators of microRNAs identified by high-throughput screen coupled with high-throughput sequencing. Nat Commun. 2023;14:7575. https://doi.org/10.1038/s41467-023-43293-0.
8. Yang T, Zhang M, Zhang N. Modified Northern blot protocol for easy detection of mRNAs in total RNA using radiolabeled probes. BMC Genomics. 2022;23:66. https://doi.org/10.1186/s12864-021-08275-w.
9. Labib M, Berezovski MV. Electrochemical sensing of microRNAs: avenues and paradigms. Biosens Bioelectron. 2015;68:83–94. https://doi.org/10.1016/j.bios.2014.12.026.
10. Wang Z-Y, Sun M-H, Zhang Q, Li P-F, Wang K, Li X-M. Advances in point-of-care testing of microRNAs based on portable instruments and visual detection. Biosensors. 2023;13:747. https://doi.org/10.3390/bios13070747.
11. Tavallaie R, De Almeida SRM, Gooding JJ. Toward biosensors for the detection of circulating MICRORNA as a cancer biomarker: an overview of the challenges and successes. WIREs Nanomed Nanobiotechnol. 2015;7:580–92. https://doi.org/10.1002/wnan.1324.
12. Kumari R, Mendki N, Chandra P. Smartphone-integrated automated sensor employing electrochemically engineered 3D bimetallic nanoflowers for hydrogen peroxide quantification in milk. Langmuir. 2024;40:11146–59. https://doi.org/10.1021/acs.langmuir.4c00726.
13. Ranjan Srivastava V, Kumari R, Chandra P. Miniaturized surface engineered technologies for multiplex biosensing devices. Electroanalysis. 2023;35:e202200355. https://doi.org/10.1002/elan.202200355.
14. Kumari R, Sammi A, Srivastava A, Azad UP, Chandra P. Emerging 3D nanomaterials as electrocatalysts for water splitting reactions. Int J Hydrogen Energy. 2024;74:214–31. https://doi.org/10.1016/j.ijhydene.2024.06.014.
15. Zhuang J, Wan H, Zhang X. Electrochemical detection of miRNA-100 in the sera of gastric cancer patients based on DSN-assisted amplification. Talanta. 2021;225: 121981. https://doi.org/10.1016/j.talanta.2020.121981.
16. Medetalibeyoglu H, Kotan G, Atar N, Yola ML. A novel and ultrasensitive sandwich-type electrochemical immunosensor based on delaminated MXene@AuNPs as signal amplification for prostate specific antigen (PSA) detection and immunosensor validation. Talanta. 2020;220:121403. https://doi.org/10.1016/j.talanta.2020.121403.
17. Yan Z, Li Y, Wei X, Li P, Jiang J, Chen Y, Duan P, Wang X, Deng P, Liu X. Sensitive photoelectrochemical biosensors based on AuNPs/MXenes electrode coupled with light-harvesting UiO-66-NH2 probes for protein kinase detection. Biosens Bioelectron X. 2022;11:100204. https://doi.org/10.1016/j.biosx.2022.100204.
18. Meng G, Long F, Zeng Z, Kong L, Zhao B, Yan J, Yang L, Yang Y, Liu X-Y, Yan Z, Lin N. Silk fibroin based wearable electrochemical sensors with biomimetic enzyme-like activity constructed for durable and on-site health monitoring. Biosens Bioelectron. 2023;228:115198. https://doi.org/10.1016/j.bios.2023.115198.
19. Selvi SV, Prasannan A, Yu H, Lincy V, Hong P-D. Bio-mineralized tin/bismuth oxide nanoparticles with silk fibroins for efficient electrochemical detection of 2-nitroaniline in river water samples. Environ Res. 2023;221:115285. https://doi.org/10.1016/j.envres.2023.115285.

20. Wang J-Y, Chen L-J, Zhao X, Yan X-P. Silk fibroin-based colorimetric microneedle patch for rapid detection of spoilage in packaged salmon samples. Food Chem. 2023;406:135039. https://doi.org/10.1016/j.foodchem.2022.135039.
21. Gao Q, Agarwal S, Greiner A, Zhang T. Electrospun fiber-based flexible electronics: fiber fabrication, device platform, functionality integration and applications. Prog Mater Sci. 2023;137:101139. https://doi.org/10.1016/j.pmatsci.2023.101139.
22. Molinnus D, Drinic A, Iken H, Kröger N, Zinser M, Smeets R, Köpf M, Kopp A, Schöning MJ. Towards a flexible electrochemical biosensor fabricated from biocompatible *Bombyx mori* silk. Biosens Bioelectron. 2021;183:113204. https://doi.org/10.1016/j.bios.2021.113204.
23. Kaur H, Chittineedi P, Bellala RS, Bellala VM, Singh S, Kumari R, Chandra P, Pandrangi SL, Singh SP. Clinically deployable bioelectronic sensing platform for ultrasensitive detection of transferrin in serum sample. Biosensors. 2023;13:406. https://doi.org/10.3390/bios13030406.
24. Mahato K, Baranwal A, Kumari R, Srivastava A, Pratap Azad U, Chandra P. Differential electrochemical behaviour of phytofabricated and chemically synthesized silver nanoparticles towards hydrogen peroxide sensing. Electroanalysis. 2023;35:e202300094. https://doi.org/10.1002/elan.202300094.
25. Kumari R, Singh A, Azad UP, Chandra P. Insights into the fabrication and electrochemical aspects of paper microfluidics-based biosensor module. Biosensors. 2023;13:891. https://doi.org/10.3390/bios13090891.
26. Yin H, Ai S, Shi W, Zhu L. A novel hydrogen peroxide biosensor based on horseradish peroxidase immobilized on gold nanoparticles–silk fibroin modified glassy carbon electrode and direct electrochemistry of horseradish peroxidase. Sens Actuators B Chem. 2009;137:747–53. https://doi.org/10.1016/j.snb.2008.12.046.
27. Kumari R, Chandra P. Electrochemical nano-imprinting of trimetallic dendritic surface for ultrasensitive detection of cephalexin in pharmaceutical formulations. Pharmaceutics. 2023;15:876. https://doi.org/10.3390/pharmaceutics15030876.
28. Kumari R, Harika GVS, Lavudi K, Josthna P. Anti-tumor activity of eco-friendly AgNPs derived from musa paradisiaca pseudo stem methanolic extracts and their antibacterial and antioxidant activities in ovarian cancer cell line-PA. Eng Technol. 2021. https://doi.org/10.22214/ijraset.2021.39285.
29. Khan R, Radoi A, Rashid S, Hayat A, Vasilescu A, Andreescu S. Two-dimensional nanostructures for electrochemical biosensor. Sensors. 2021;21:3369. https://doi.org/10.3390/s21103369.
30. Liu XQ, Picart C. Layer-by-layer assemblies for cancer treatment and diagnosis. Adv Mater. 2016;28:1295–301. https://doi.org/10.1002/adma.201502660.
31. Cai J, Zhang L, Chang C, Cheng G, Chen X, Chu B. Hydrogen-bond-induced inclusion complex in aqueous cellulose/LiOH/urea solution at low temperature. ChemPhysChem. 2007;8:1572–9. https://doi.org/10.1002/cphc.200700229.
32. Jiang J, Luo L, Ying N, Wu S, Ji J, Su H, Li X, Zeng D. Electrochemical biosensor based on PAMAM functionalized MXene nanoplatform for detection of folate receptor. Bioelectrochemistry. 2024;156:108627. https://doi.org/10.1016/j.bioelechem.2023.108627.
33. Woo J, Na Y, Choi WI, Kim S, Kim J, Hong J, Sung D. Functional ferrocene polymer multilayer coatings for implantable medical devices: biocompatible, antifouling, and ROS-sensitive controlled release of therapeutic drugs. Acta Biomater. 2021;125:242–52. https://doi.org/10.1016/j.actbio.2021.02.038.
34. Cao S, Wu H, Pijpers IAB, Shao J, Abdelmohsen LKEA, Williams DS, Van Hest JCM. Cucurbit-like polymersomes with aggregation-induced emission properties show enzyme-mediated motility. ACS Nano. 2021;15:18270–8. https://doi.org/10.1021/acsnano.1c07343.
35. Zhang Y, Zhang Z, Wang Z, Pan H, Lin Y, Chang D. Sensitive detection of prostate-specific antigen based on dual signal amplification of Fc@MgAl-LDH and NH2-MIL-101(Fe). Biosens Bioelectron. 2021;190:113437. https://doi.org/10.1016/j.bios.2021.113437.
36. Sun W, Zhang J, Xie M, Lu D, Zhao Z, Li Y, Cheng Z, Zhang S, Chen H. Ultrathin aramid/COF heterolayered membrane for solid-state Li-metal batteries. Nano Lett. 2020;20:8120–6. https://doi.org/10.1021/acs.nanolett.0c03133.
37. Ma Y, Li M, Zhang Y. Ratiometric electrochemical biosensor based on hybridization chain reaction signal amplification for sensitive microRNA-155 detection. Anal Methods. 2024;16:5032–7. https://doi.org/10.1039/D4AY00868E.
38. Du S, Xie B, Gao H, Zhang J, Fu H, Liao F, Liao Y. Self-powered DNAzyme walker enables dual-mode biosensor construction for electrochemiluminescence and electrochemical detection of microRNA. Anal Chem. 2023;95:7006–13. https://doi.org/10.1021/acs.analchem.3c00546.
39. Liu S, Jiang X, Wan F, Jia S, Si S. A novel detection of MicroRNA based on homogeneous electrochemical sensor with enzyme-assisted signal amplification. Talanta. 2023;256:124263. https://doi.org/10.1016/j.talanta.2023.124263.
40. Wang H, Li H, Huang Y, Xiong M, Wang F, Li C. A label-free electrochemical biosensor for highly sensitive detection of gliotoxin based on DNA nanostructure/MXene nanocomplexes. Biosens Bioelectron. 2019;142:111531. https://doi.org/10.1016/j.bios.2019.111531.
41. Yao Y, Pan H, Luo Y, Zhu D, Chao J, Su S, Wang L. A label-free electrochemical sensor for ultrasensitive microRNA-21 analysis based on the poly(L-cysteine)/MoS_2 sensing interface. Analyst. 2021;146:1663–7. https://doi.org/10.1039/D0AN02314K.
42. Kong L, Lv S, Qiao Z, Yan Y, Zhang J, Bi S. Metal-organic framework nanoreactor-based electrochemical biosensor coupled with three-dimensional DNA walker for label-free detection of microRNA. Biosens Bioelectron. 2022;207:114188. https://doi.org/10.1016/j.bios.2022.114188.